PCCP

ROYAL SOCIETY OF CHEMISTRY

PAPER

View Article Online
View Journal | View Issue

Cite this: *Phys. Chem. Chem. Phys.*, 2022, **24**, 13922

Growth and characterization of melem hydrate crystals with a hydrogen-bonded heptazine framework†

Tomonori Dai,[a] Hiroki Kiuchi,[a] Hiroki Minamide,[a] Yuto Miyake,[a] Hiroya Inoki,[a] Yoriko Sonoda,[b] Jun'ya Tsutsumi[b] and Kaname Kanai *[a]

In carbon nitride (CN) compounds, hydrogen bonds play a major role in cohesion, in addition to dispersion forces. The crystal structures of CN compounds produced *via* thermal polymerization are complex, but they possess unique and attractive features. Melem is a well-known building unit of CN compounds such as melon and g-C_3N_4, which have recently attracted attention as photocatalysts. Melem hydrate (Mh) forms hexagonal prismatic crystals that are sufficiently porous to accommodate small molecules. In this study, we grew and characterized single crystals of Mh and investigated their optical properties and hygroscopicity. By precisely adjusting the hydration conditions, we succeeded in growing a well-formed hexagonal prismatic single crystal of Mh (Mhr) with a length measuring several tens of micrometers. Furthermore, we discovered a parallelogram-shaped Mh single crystal (Mhp), which possessed a different crystal structure and optical properties from those of Mh and melem crystals. Although the crystal structure of Mh was greatly disrupted by dehydration, it exhibited hygroscopicity and could absorb moisture even in air, restoring the crystal structure of Mh. In addition, Mh demonstrated a high photoluminescence quantum yield and long lifetime delayed fluorescence, similar to melem crystal. The high quantum yield of Mh can be attributed to the effect of the strong anchoring of the melem molecule by several hydrogen bonds in the Mh crystal, since the strongly anchored molecule is less likely to undergo radiation-free deactivation due to the small displacement of atomic positions in the excited state after light absorption. The findings obtained in this study shed light not only on the application of CN compounds as photocatalysts, but also on a wider range of applications based on their optoelectronic functions.

Received 11th February 2022,
Accepted 13th May 2022

DOI: 10.1039/d2cp00691j

rsc.li/pccp

1. Introduction

In recent years, carbon nitride (CN) compounds have attracted considerable attention as photocatalysts that can decompose water to generate hydrogen mainly using visible light.[2] Following the pioneering work of Wang *et al.*, numerous studies conducted on graphitic CN (g-CN) have led to the development of new CN compounds.[3] For example, the formation of g-C_3N_4 and g-C_6N_6 has been theoretically predicted, while melon and graphitic s-triazine based C_3N_4 (gt-C_3N_4) has been synthesized.[4–7] Hydrogen bonds play an important role in the formation of complex and diverse crystal structures in some CN compounds. For example, the CN polymer called "melon" is one of the representative g-CN compounds that are widely studied in the field of photocatalysis. Melon has a layered structure, consisting of melem molecules (Fig. 1) that are polymerized in one-dimensional chains, forming two-dimensional layers *via* hydrogen bonding and dispersion forces.[6,8–11] Although its structure is essentially different from the two-dimensional polymeric structure of g-C_3N_4, many papers written since the early stages of g-CN research to the present have mistaken melon for g-C_3N_4.[11–13] Due to the structural difference between melon and g-C_3N_4, melon possesses an energy band structure with a direct energy gap,[14] as opposed to that of g-C_3N_4 with an indirect gap. The direct energy gap of melon promotes the quenching of excitons after light is absorbed and reduces the charge separation efficiency, resulting in low photocatalytic activity. In view of this, numerous research works have been performed to improve the photocatalytic activity of melon *via* various efforts, such as by increasing its effective surface area.

[a] *Department of Physics, Faculty of Science and Technology, Tokyo University of Science, 2641 Yamazaki, Noda, Chiba 278-8510, Japan. E-mail: kaname@rs.tus.ac.jp*
[b] *Research Institute for Advanced Electronics and Photonics, National Institute of Advanced Industrial Science and Technology (AIST), Higashi 1-1-1, 305-8565 Tsukuba, Ibaraki, Japan*

† Electronic supplementary information (ESI) available. See DOI: https://doi.org/10.1039/d2cp00691j

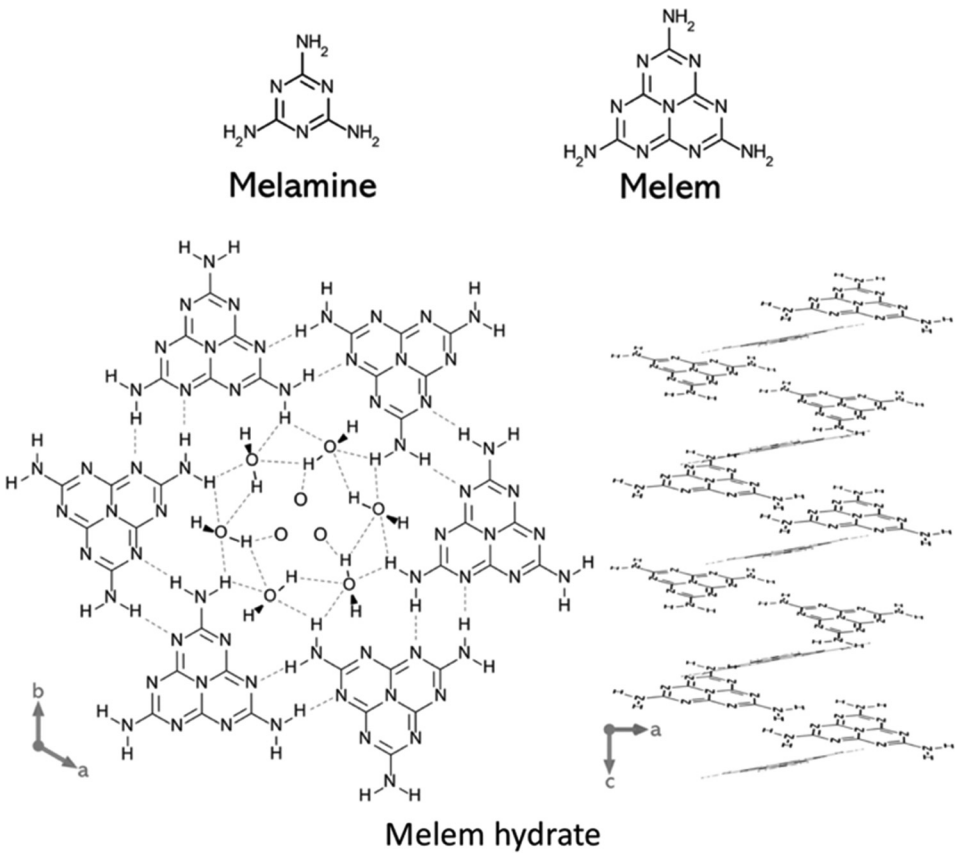

Fig. 1 Molecular structures of melamine, melem, and melem hydrate (Mh). The bottom left of the figure shows the arrangement of melem molecules in the *ab*-plane perpendicular to the channel extending in the *c*-axis direction. Six melem molecules are arranged in a helix motif *via* hydrogen bonds along the *c*-axis, resulting in a corrugated layer. The channel is filled with water.[1] The dashed lines represent hydrogen bonds. The bottom right of the figure shows the arrangement of melem molecules in helical structures along the *c*-axis.

However, the electronic structure of melon limits its ability to work as a photocatalyst on its own. Since melon emits blue fluorescence, as expected from its energy band structure,[15,16] it can be applied as a light-emitting layer that emits blue light in a light-emitting device. Melem, the constituent unit of melon, also emits fluorescence in the near-ultraviolet (UV) region at a very high quantum efficiency.[16–18] This high quantum efficiency is believed to be caused by the thermally activated delayed fluorescence (TADF) process.[19–21] Over the last decade, CN compounds have garnered attention as materials for various technological applications due to their high stability against heat and oxidation, as well as their properties as semiconductors. In addition to their photocatalytic properties, melon and melem are chemically robust, making them attractive semiconductors that exhibit optoelectronic functions. In fact, the fabrication of a light-emitting diode using melon or melem thin films as the light-emitting layer has recently been reported.[22] Near-UV luminescence similar to that emitted by melem has the potential to be applied not only to novel optoelectronic devices but also to the sterilization technology and medical fields.[23] UV-light-emitting diodes are also expected to be applied for information storage applications and backlight sources for full-color displays.[24]

Crystals of melem (*c*-melem) are known to exhibit a monoclinic structure that is aggregated by hydrogen bonds and intermolecular interactions between the CN heterocyclic ring and amino groups.[8,25,26] Melem can be synthesized inexpensively *via* the thermal polymerization method using melamine (Fig. 1)[27–29] and dicyandiamide[30] as the starting materials. This method has led to the development of new materials using melem as the building unit in recent years.[31] Melem is also known to produce hydrates *via* relatively simple methods such as hydrothermal and ultrasonic treatments.[1] The melem hydrothermal method conducted at 200 °C has been reported to produce porous melem hydrate (Mh) crystals in a hexagonal prism shape possessing hexagonal channels with diameters as large as 0.89 nm.[1] The resulting Mh exhibits a complex crystal structure due to the hydrogen bonds between the water and melem molecules, as shown in Fig. 1. In the Mh crystal, six melem molecules are arranged in a helix motif *via* hydrogen bonds along the *c*-axis, resulting in a corrugated-layered hexagonal channel that is filled with randomly coordinated water molecules.[1] Besides hydrates, melamine and cyanuric acid compounds are also self-assembled CN compounds produced *via* hydrogen bonding with other small molecules.[32] Mh has been identified as the precursor of porous melon in previous studies.[33–35] In fact, most previous studies on Mh have focused on

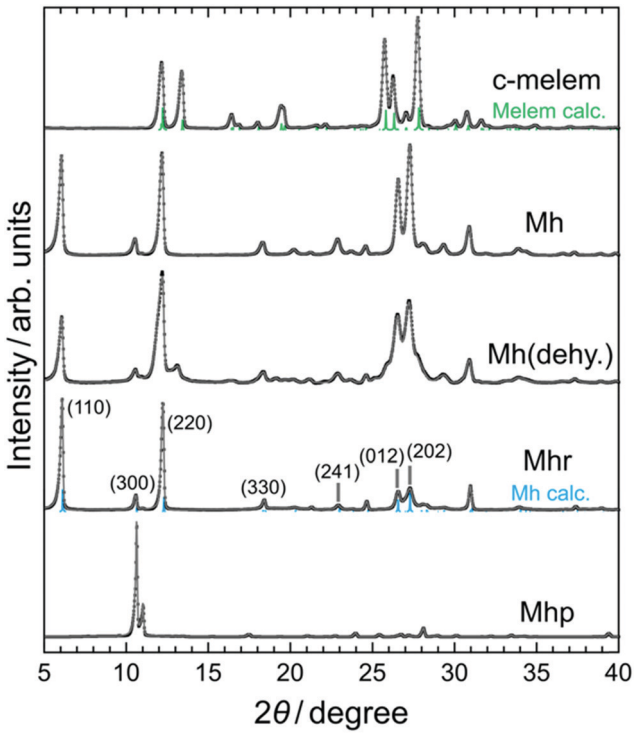

Fig. 2 XRD profiles of c-melem, Mh, Mh(dehy.), Mhr, and Mhp powder samples. The green and blue vertical bars represent the simulated diffraction peaks for c-melem and Mhr crystals, respectively.

the photocatalytic activity of porous melons obtained by Mh calcination, while the structure and properties of Mh have not been reported in detail. Investigating the structure and fundamental properties of Mh, which possesses a unique and complex crystal structure, provides a deep insight into the role of hydrogen bonding in the crystals of CN compounds. Among the various self-assembled CN compounds, only a few, such as Mh, constitute large channels.[32,36,37]

In this study, Mh was synthesized, and its fundamental physical properties were evaluated as a basis for applied research on Mh itself. Rod-shaped Mh (Mhr) single crystals with smooth surfaces and sizes suitable for optoelectronic devices[38–44] were grown *via* the poor solvent vapor diffusion method[45–47] and water content control. The luminescence properties of Mh were then evaluated by comparing their optical properties with those of c-melem. The hygroscopicity of Mh was also evaluated. In addition, parallelogram-shaped Mh (Mhp) composed of a different number and configuration of water molecules compared to Mhr, was newly discovered, and its optical and thermal behaviors were investigated. Table 1 lists the abbreviations for the substances in this paper.

Table 1 Abbreviations for the substances in this paper

Abbreviation	Substances
c-Melem	Melem crystal
Mh	Melem hydrate
Mhr	Rod-shaped Mh single crystal
Mh(deny.)	Dehydrated Mh
Mhp	Parallelogram-shaped Mh single crystal

2. Experimental and calculation methods

2.1. Synthesis of c-melem

5 g of melamine (purity: 99.0%; FUJIFILM Wako Pure Chem. Co., Ltd; 139-00945) was synthesized in a tube furnace (KTF035N1; Koyo Thermo Systems Co., Ltd) under an N_2 atmosphere (purity: 99.99995%).[13] The temperature of the material was raised from room temperature at 1 °C min^{-1} and maintained at 310 °C for 5 h. The material was then cooled naturally to obtain melem. 500 mg of the as-synthesized melem was washed with 50 ml of *N*,*N*-dimethylformamide (DMF; purity: 99.5%; FUJIFILM Wako Pure Chem. Co., Ltd; 045-02916) in which melamine is easily soluble and melem is less soluble.[48,49] Sonication and centrifugation were conducted twice for 15 min before 50 ml of acetone (purity: 99.5%; FUJIFILM Wako Pure Chem. Co., Ltd; 012-00343)[50] was added to remove DMF. This was followed by two sets of 15 min sonication at 42 kHz and centrifugation at about 2500 rpm. Then, the powdery melem sample was dried by heating at 150 °C for 24 h to obtain c-melem as the starting material for the growth of Mh crystals.

2.2. Preparation of Mh

250 mg of c-melem was sonicated with 50 ml of pure water (FUJIFILM Wako Pure Chem. Co., Ltd; 161-08247) or deuterium oxide (purity: 99.8%; FUJIFILM Wako Pure Chem. Co., Ltd; 7789-20-0) at 42 kHz for 15 min twice in order to completely disperse the powdery c-melem. The material was then rinsed with acetone and dried in air to obtain Mh.

2.3. Preparation of dehydrated Mh (Mh(dehy.))

Mh was annealed at 150 °C for 24 h and cooled in air to obtain Mh(dehy.). The initial temperature for annealing is room temperature. The Mh(dehy.) samples used in the hygroscopicity experiments were not cooled in air after annealing. Instead, they were immediately transferred to a vacuum container for storage to avoid exposure to air. Sample Mh(dehy.)(atm., 1 w) was prepared by leaving Mh(dehy.) at room temperature and 45% humidity for one week. Sample Mh(dehy.)(water, 1 h) was prepared by immersing approximately 30 mg of Mh(dehy.) in 100 ml of pure water at room temperature for 1 h.

2.4. Single-crystal growth of Mhr

15 mg of c-melem was added to 30 ml of super dehydrated dimethyl sulfoxide (DMSO, s. d.; purity: 99.0%; FUJIFILM Wako Pure Chem. Co., Ltd; 040-32815). The mixture was dissolved by sonication at 42 kHz for 15 min.[51] 2 ml of the melem solution was transferred into a 6 ml screw tube using a syringe, and 100 μl of pure water was injected into the tube using a micropipette. The solution was sonicated at 42 kHz for 15 min to disperse pure water into the solution. The screw tube containing the solution was placed in a 20 ml snap cup containing 4 ml of MeOH and covered with a lid. Single crystals were grown *via* the poor solvent vapor diffusion method in the dark at room temperature for 7 d.[45–47] Mhr was annealed at 150 °C for 24 h and cooled in air to obtain dehydrated Mhr.

2.5. Single-crystal growth of parallelogram-shaped Mh (Mhp)

45 mg of c-melem was dissolved in 30 ml of DMSO, s. d. by sonication at 42 kHz for 15 min. The melem solution was transferred into a 6 ml screw tube using a 2 ml syringe, and 200 μl of pure water was added into the tube using a micropipette. The solution was sonicated at 42 kHz for 15 min to disperse water into the solution and further cloud the melem solution. The screw tube containing the solution was placed in a 20 ml-snap cup containing 4 ml of MeOH and covered with a lid. Single crystals were grown *via* the poor solvent vapor diffusion method in the dark at room temperature for 7 d. The samples were prepared by heating Mhp at 130 °C for 1 h followed by cooling, and by heating Mhp at 200 °C for 3 h followed by cooling.

2.6. Characterization

Osmium-coated samples were used for scanning electron microscopy (SEM; FE-SEM SUPRA40; Carl Zeiss). The osmium coating was performed with a coater (Neoc-Pro; MEIWAFOSIS, Ltd) using osmium(VIII) oxide (purity: 99.8%; FUJIFILM Wako Pure Chem. Co., Ltd; 157-00404). Twisted Mhr (Mhr(dehy.)) was attached to a carbon tape, annealed at 150 °C for 24 h and cooled in air.

Powder X-ray diffraction (XRD) analyses were conducted using a diffractometer (Ultima IV, Rigaku) with a Cu Kα radiation source (λ = 1.5418 Å).

Thermogravimetry-differential thermal analysis (TG-DTA) measurements were performed using TG-DTA2010SA (Bruker XS). TG-DTA curves were acquired in a dry N_2 atmosphere at a heating rate of 5 °C min^{-1}.

Photoluminescence (PL) spectra and absolute PL quantum yields of the powdered samples were measured using a spectrometer (Quantaurus-QY, C11347-01; Hamamatsu Photonics, Ltd) with samples in quartz Petri dishes (A10095-03; Hamamatsu Photonics, Ltd).

Ultraviolet-visible (UV-Vis) spectra of the powder samples were obtained using U-4100 (HITACHI). Pellets of the samples were prepared by mixing KBr powder (FUJIFILM Wako Pure Chem. Co., Ltd; 165-1711) and pressurizing at 10 MPa. The UV-vis data were acquired using a UV-vis spectrometer (U-4100, HITACHI).

The sample for fluorescence lifetime measurements was prepared by sandwiching a powder sample between two quartz plates. The measurements were carried out using a compact fluorescence lifetime measurement system (Quantaurus-Tau, C11367-01; Hamamatsu Photonics, Ltd). The excitation light wavelength used to perform the measurements was 340 nm. The monitored emission wavelengths for c-melem, Mh(dehy.), Mhr, and melem(DMSO) were set to 370 nm; and that of Mhp was set to 380 nm.

2.7. Calculation method

XRD profiles were calculated using the powder diffraction pattern package by employing the Visualization for Electronic and Structural Analysis (VESTA) program. The structures of c-melem and Mhr reported in previous studies were used.[8,17]

The energy bands were calculated based on the density functional theory (DFT). The calculations were performed using the CASTEP[52] plane wave basis set and general gradient approximation (GGA) applying Perdew–Burke–Ernzerhof (PBE) as the correlation functional[53] (Dassault SystemesBIOVIA).[54] The details of the calculation are as follows, energy cutoff: 789.1000 eV, SCF tolerance threshold: 2.0×10^{-6} eV per atom, *k*-point set in reciprocal space: (separation: 0.08 $Å^{-1}$, Monkhorst–Pack grids: 1 × 1 × 2), pseudopotentials: norm conserving, finite basis set correction: not used, and dispersion correction: not used. The calculations were performed using the c-melem and Mhr structures reported in previous studies;[55,56] for the Mhr structure, the *c*-axis was adjusted to be 0.13 Å longer to better reproduce the XRD data. The obtained atomic coordinates of Mhr are shown in Table S1 in the ESI.†

3. Results and discussion

3.1. Crystal structures of c-melem and Mh

The XRD profiles of c-melem and Mh were in good agreement with previously reported data,[1,8] indicating that the compounds were successfully synthesized. Mh, Mh(dehy.), and Mhr showed the same diffraction peaks. The Mh powder sample was composed of rod-like microcrystals, and the only difference between Mh and Mhr was the size of the crystals. The simulated XRD profile of the Mh crystal was used to assign the peaks in the Mhr data and to determine the indices. The results are summarized in Table 2. The (110) and (220) diffraction peaks in the *ab*-plane of Mh(dehy.) were similar to those of Mh, indicating that the crystal structure in the *ab*-plane was maintained after dehydration. In contrast, the (012) and (202) peaks in Mh(dehy.) assigned to interlayer diffraction broadened and their intensities were reduced, indicating that the interlayer structure was greatly disrupted by dehydration. However, the shapes and intensities of the peaks observed in this study were relatively better preserved compared to those reported in a previous study,[1] suggesting that water vapor might have been included in the structure when it

Table 2 Crystal structures of c-melem, Mh, Mh(dehy.), and Mhr derived from the XRD results

Sample	Crystal system	Space group	*a*/Å	*b*/Å	*c*/Å	α/°	β/°	γ/°	Ref.
c-Melem	Monoclinic	$P2_1/c$ (no. 14)	7.3992	8.6528	13.3816	90	99.912	90	7
Mh	Trigonal	$R\bar{3}c$ (no. 167)	28.790(4)	28.790(4)	6.6401	90	90	120	31
Mh(dehy.)	Trigonal	$R\bar{3}c$ (no. 167)	28.790(4)	28.790(4)	6.7876	90	90	120	This work[a]
Mhr	Trigonal	$R\bar{3}c$ (no. 167)	28.790(4)	28.790(4)	6.7728	90	90	120	This work[a]

[a] Obtained by analyzing the XRD results in Fig. 2, showing a slight difference from the crystal structures reported in previous studies.[1,8]

was cooled in air after dehydration. This indicated that Mh could be rehydrated to some extent, even after dehydration, as discussed in section 3.4.

The XRD profiles of Mhp were completely different from those of the other samples, suggesting that the newly discovered Mh crystal exhibited a completely different crystal structure from that of Mh. Fig. 3 shows the SEM images of c-melem, Mh, Mhr, and Mhp crystals. The c-melem powder showed an angular shape (Fig. 3(a)), whereas the Mh powder showed a rod-like shape (Fig. 3(b)).

c-Melem exhibited a monoclinic structure whereas Mh exhibited a hexagonal structure. As shown in Fig. 3(b), Mh microcrystals that clearly showed the shape of a hexagonal prism were hardly observed. Instead, we obtained rod-shaped crystals that grew into larger single crystals. This rod-shaped Mh crystal of Mh was referred to as Mhr in this study. Fig. 3(c) shows an Mhr crystal with length measuring tens of micrometers and diameter measuring a few micrometers. Based on the SEM images, rod-shaped single crystals with well-defined surfaces and shapes, an average length $L = 89.6 \pm 51.3$ μm (for 10 units of crystals) and a diameter $d = 3.7 \pm 1.8$ μm were observed. From the XRD measurements, the interlayer distance along the *c*-axis of the obtained Mhr crystals was approximately 0.13 Å longer than that reported previously.[1] The obtained atomic coordinates of Mhr are shown in Table S1 (ESI†). Furthermore, the obtained Mhr was confirmed to be the single crystal of Mh, since complete quenching could be observed at every 90° rotation of the crystal under the crossed Nicol condition of the polarized light microscope, as shown in Fig. S1 in the ESI.†[57] The average L value of Mhr was over 50 μm, easing the attachment of electrodes to the crystals, thus making them suitable for use in electronic devices.[38–44]

Mhr was confirmed to be twisted when annealed at 150 °C for 24 h. Although we did not strictly observe the heating-induced deformation of a specific Mhr, the SEM images clearly depicted twisted hexagonal prisms after annealing. Wrinkles were observed in the conductive tape, where the crystal was fixed, as shown in Fig. 3(e), clearly indicating that the crystal was twisted after annealing. From the XRD results, the (012) and (202) peaks of Mh(dehy.), which were attributed to interlayer-derived diffractions, were shifted to 0.1° lower compared to those of Mh, suggesting that the *c*-axis distance of the unit cell increased and the average intermolecular distance became slightly larger in the twisted Mhr. In other words, as the distance between the unit cells in the *c*-axis direction increased, the melem molecules moved slightly to fill the space in the crystal vacated by dehydration, leading to a reduction in crystal volume.

By increasing the amount of water used to grow Mhr crystals by 5%, a completely different crystal phase was grown. Fig. 3(f and g) show the SEM images of the new Mhp crystal, which exhibited a parallelogram shape with well-defined faces. The average length of the long side was $l = 20.4 \pm 4.1$ μm and that of the short side was $s = 14.2 \pm 2.1$ μm. Studies have shown that molecular crystals of various shapes can be formed by adjusting the ratio and amount of good and poor solvents. One such example is the formation of rod- and cube-shaped C_{70} fullerene. Consistent with these studies,[58,59] the different solution growth conditions used in the current study resulted in different shapes of Mhp single crystals grown. The XRD profile of Mhp suggested that its crystal structure was neither that of c-melem nor Mhr. While a previous study[34] has proven that the XRD profile of c-melem depicted diffraction peaks which resembled those of Mhp, the existence of a new hydrate is yet to be pointed out.

3.2. Chemical states and thermal behaviors of c-melem and Mh

The Fourier-transform infrared (FTIR) spectrum of the purified c-melem shown in Fig. 4(a) demonstrates absorption peaks originating from the NH stretching vibration at 3400–3600 cm^{-1}, specifically the two characteristic peaks at 3427 and 3487 cm^{-1}, and stretching vibrations of CN groups in the heterocyclic ring at

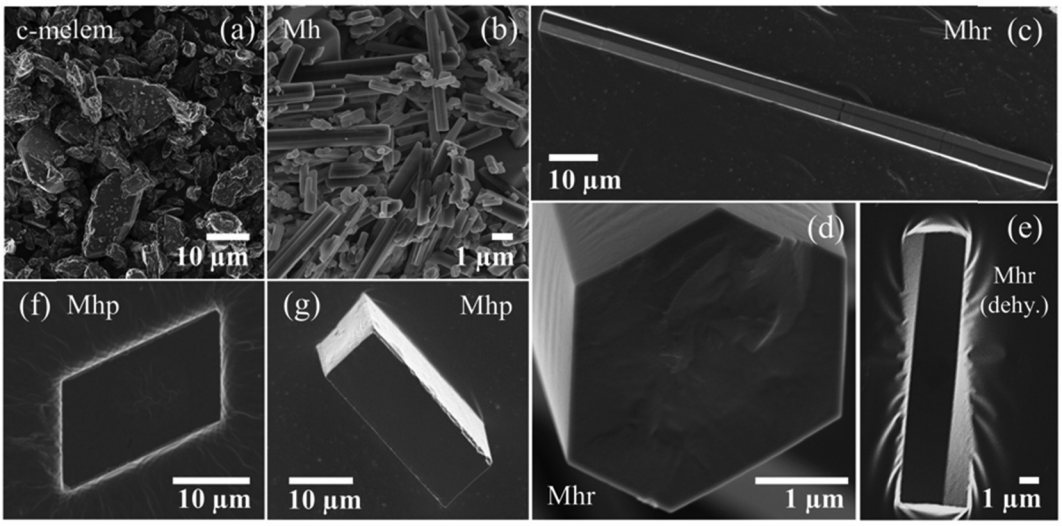

Fig. 3 SEM images of (a) c-melem, (b) Mh, (c and d) Mhr, (f and g) Mhp, and (e) Mhr annealed at 150 °C for 24 h.

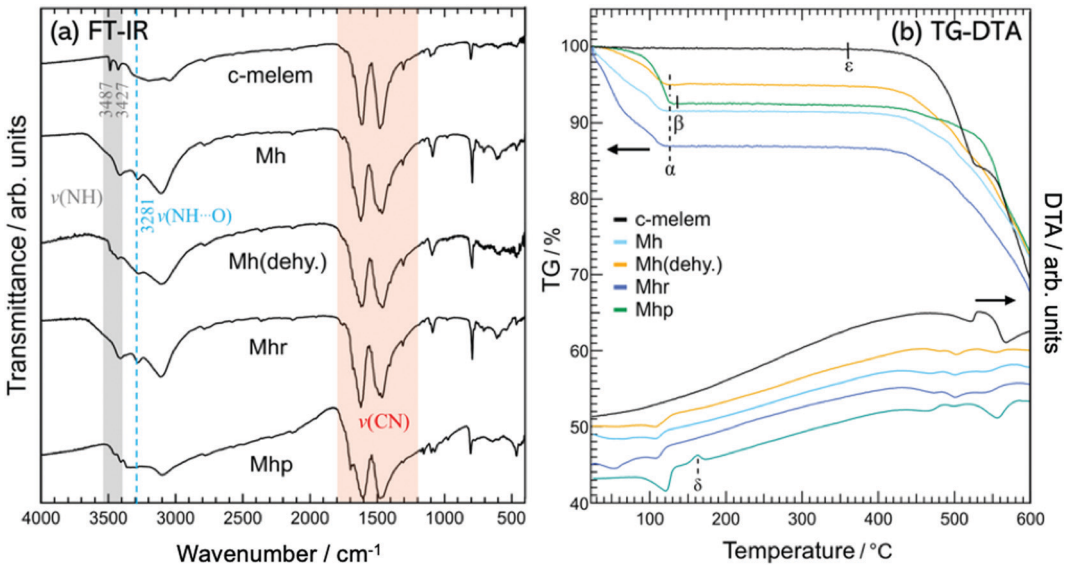

Fig. 4 (a) FTIR spectra and (b) TG-TDA data of c-melem, Mh, Mh(dehy.), Mhr, and Mhp. The upper half of (b) depicts mass loss as a function of temperature, in which the vertical axis on the left shows the ratio of mass loss. The lower half of (b) depicts differential heat as a function of temperature, in which the downward peak represents the heat absorption of the sample while the upward peak represents the heat generation of the sample.

1200–1800 cm^{-1}, which are similar in shape to those of c-melem reported in a previous study.[8] These observations confirmed the proper synthesis of c-melem. Since all the samples shown in Fig. 4(a) used melem molecules as their constituent units, the absorption peaks originating from the stretching vibration of the CN group of the heterocyclic ring were also similar in structure. As a result, it was difficult to extract information about the differences in the chemical environments of each sample from these peaks. From the TG-DTA results shown in Fig. 4(b), the mass loss of c-melem when heated from room temperature to 360 °C was only 0.34%, indicating that the desorption of melamine, which was contained in the unreacted residue during the synthesis of c-melem, had hardly occurred. From the mass loss results, the existence molar ratio of melamine to melem was calculated to be 5.82×10^{-3}, indicating that c-melem with a very high purity of 99.6% was obtained in this study. Based on the FTIR spectrum of Mh shown in Fig. 4(a), the ν(NH···O) stretching vibration of the NH groups of melem appeared at 3281 cm^{-1}, suggesting a lower energy than that of c-melem due to the hydrogen bond formed between the NH group of melem with water molecules. The absorption peaks attributed to the stretching vibration of NH groups at 3400–3600 cm^{-1} and CN groups at 1200–1800 cm^{-1} were similar to those observed in the FTIR spectra of Mh reported in previous studies,[1,60] confirming that Mh was synthesized correctly in this study.

The TG-TDA results of Mh, Mh(dehy.), Mhr, and Mhp suggested mass loss and endothermy associated with dehydration, as opposed to that of c-melem. The masses of Mh, Mh(dehy.), and Mhr decreased gradually when the temperature increased from room temperature to approximately 125 °C, represented as α in Fig. 4(b). Mhp showed mass loss over a slightly larger temperature range from room temperature to approximately 135 °C, represented as β in Fig. 4(b). These mass losses were caused by the desorption of water attached to the crystal surfaces and in the crystals.[1,61] For Mh, Mh(dehy.), Mhr, and Mhp, the molar ratios of water molecules to melem molecules were calculated to be 1.11 (8.38%), 0.63 (4.96%), 1.82 (13.09%), and 0.97 (7.40%), respectively. The values in parentheses indicate the percentage of mass loss. The mass loss of water was in the increasing order of Mh(dehy.), Mh, and Mhr. The incomplete dehydration of Mh(dehy.) suggested that water in air might have been incorporated into its crystal after dehydration. The hygroscopicity of Mh(dehy.) is discussed in section 3.4. As shown in Fig. 4(b), Mh, Mh(dehy.), and Mhr did not undergo any exothermic reaction when water was desorbed at increasing temperatures, but Mhp underwent an exothermic reaction without mass loss at 162 °C, indicated by δ, which was higher than the temperature at which water was completely desorbed at 135 °C. This energy was identified as the extra energy released when the crystal transformed into a more stable structure, proving that the crystal structure had undergone a phase transition. As shown in Fig. 4(b), Mhp demonstrated a clear decrease in mass due to the desorption of water as the temperature increased. Since Mhp was a hydrate like Mh, hydrogen bonds were expected to be present between the melem molecules and water, as in Mh. However, the FTIR spectrum of Mhp in Fig. 4(a) exhibited small peaks at 3400–3600 cm^{-1} due to the stretching vibration of the NH group. In contrast, the peak at 3281 cm^{-1} attributed to the NH···O stretching vibration of hydrogen bonds with water did not appear, suggesting that the chemical state of Mhp was closer to that of c-melem than to that of Mh, and the amino groups of the melem molecules in Mhp did not bond to water in the same manner as in Mh.[1,8,55] Although the crystal structure of Mhp, including the arrangement of water molecules, is not known to date, the results shown in Fig. 4(b) suggested that

the unstable crystal structure with removed water molecules underwent a phase transition to another crystal structure at T_c = 162 °C.

To further investigate the structural phase transition of Mhp, XRD and FTIR measurements were performed at temperatures of 130 °C, which was immediately above the dehydration temperature, and 200 °C after the exothermic reaction, as shown in Fig. 5. Fig. 5 shows the powder XRD and FTIR results of Mhp at room temperature (bottom), Mhp annealed at 130 °C for 1 h (middle), and Mhp annealed at 200 °C for 3 h (top). The TG-DTA results shown in Fig. 4 indicated the structural phase transition of Mhp at T_c, while the results shown in Fig. 5 aided in the identification of the phase transitions. The XRD profile of the Mhp annealed at 200 °C for 3 h was in good agreement with that of c-melem shown in Fig. 2. Furthermore, the FTIR spectrum of Mhp annealed at 200 °C for 3 h was also the same as that of c-melem, which showed characteristic NH vibrations at 3425 and 3487 cm^{-1}, indicating that the sample was completely dehydrated. The XRD profile and FTIR spectrum of Mhp annealed at 130 °C for 1 h resulted in a mixture of contributions from Mhp and c-melem. Even though this spectrum has not been observed in previous studies, its spectral shape was similar to that obtained when treating melem with 5% water/IPA.[34] The results indicated that the exothermic reaction of Mhp shown in Fig. 4(b) at T_c was caused by the structural phase transition to c-melem after the dehydration of Mhp.

Fig. 6(a) shows the powder XRD profiles of Mh prepared using D_2O and Mh. The XRD profile of Mh prepared from D_2O ($Mh(D_2O)$) showed diffractions due to the in-plane structure (a- and *b*-axis) on the low-angle side and the out-of-plane structures (*c*-axis) at 2θ = 25–30°, which was similar to the characteristics of Mh, indicating that the crystal structure of $Mh(D_2O)$ was similar to that of Mh. This proved that Mh could be properly prepared using D_2O. Fig. 6(b) shows the FTIR spectra of $Mh(D_2O)$ and Mh. Two peaks of melem-specific CN stretching vibration at 1200–1800 cm^{-1} were observed in both spectra. However, the intensity of the NH···O vibrational peak at 3281 cm^{-1} of $Mh(D_2O)$ was lower than that of Mh,[55] D_2O-derived vibrational peaks ν(OD) at 2100–2600 cm^{-1} and δ(OD) at 1211 cm^{-1} also appeared in the spectra of $Mh(D_2O)$.[56] This indicated that the D_2O molecules were also accommodated in the channel formed along the *c*-axis of the $Mh(D_2O)$ crystal, stabilizing the crystal structure.

3.3. Optical properties of c-melem and Mh

The PL and UV-vis spectra of c-melem, Mh(dehy.), Mhr, and Mhp are shown in Fig. 7. Based on the PL spectra shown in Fig. 7(a), the wavelengths providing the maximum emission intensity were 371 nm for c-melem and Mh(dehy.), 372 nm for Mhr, and 378 nm for Mhp, suggesting that Mhp emitted at slightly longer wavelengths compared to c-melem, Mh(dehy.), and Mhr. The full width at half maximum of the PL spectrum increased in the order of c-melem (61 nm), Mh(dehy.) (67 nm), Mhr (73 nm), and Mhp (83 nm). The spectra for all the compounds except for c-melem split into two broad peaks, with Mhp having the largest splitting width. As shown in the bottom panel of Fig. 7(a), the Mhp spectrum demonstrated the longest tail, extending over wavelengths longer than 380 nm, and the highest luminescence intensity at longer wavelengths compared to the other compounds.

Based on the UV-vis spectra of the powder samples shown in Fig. 7(b), the absorption edges were observed at wavelengths of

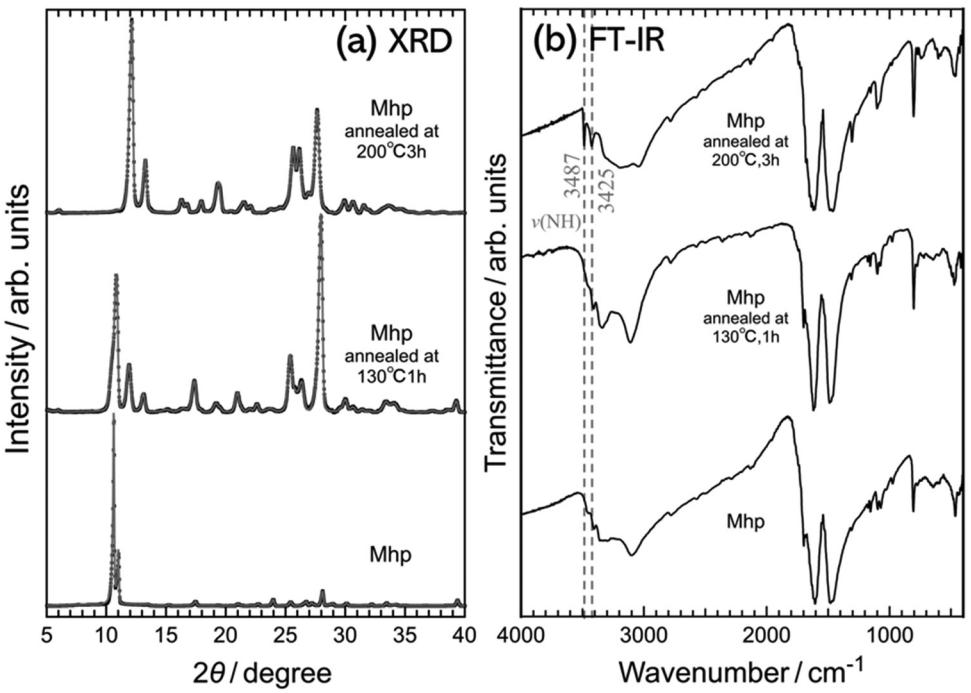

Fig. 5 (a) Powder XRD profiles and (b) FTIR spectra of Mhp (bottom), Mhp annealed at 130 °C for 1 h (middle), and Mhp annealed at 200 °C for 3 h (top).

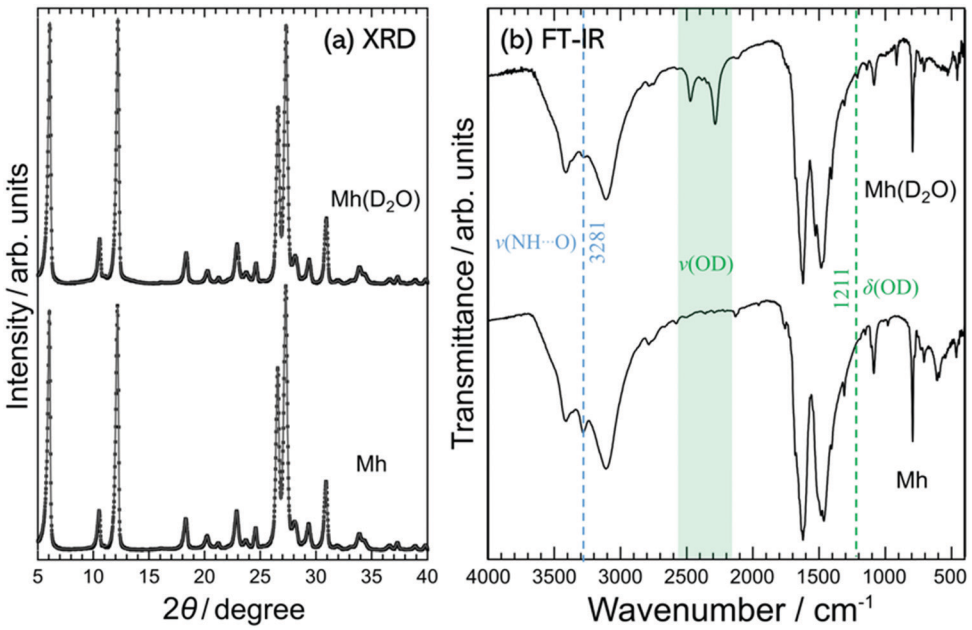

Fig. 6 (a) Powder XRD profiles and (b) FTIR spectra of Mh(D_2O) and Mh.

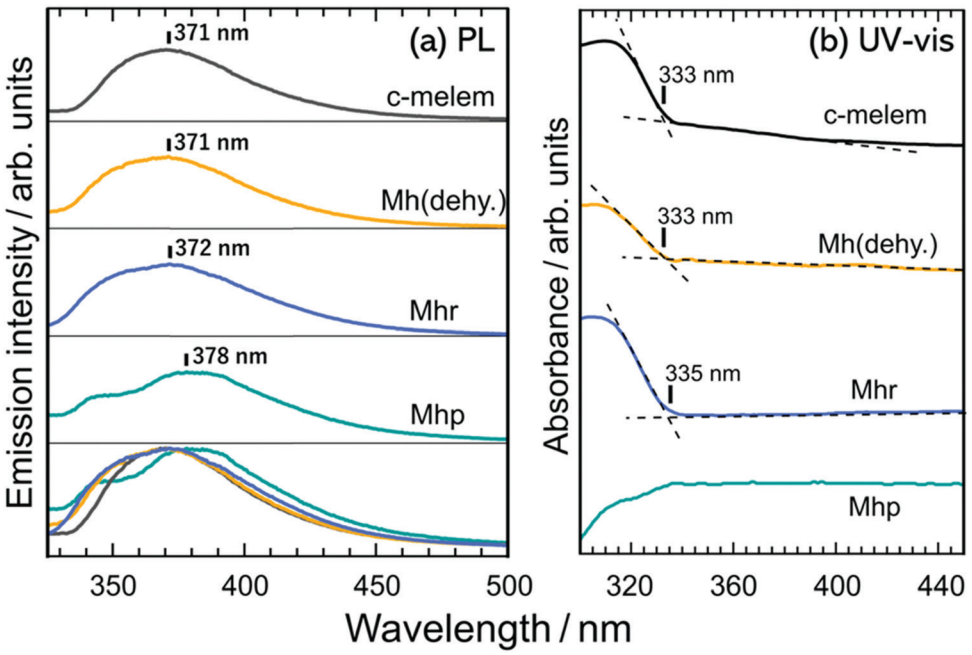

Fig. 7 (a) PL spectra of c-melem, Mh(dehy.), Mhr, and Mhp. All the spectra are superimposed at the bottom of the figure for easy comparison. (b) UV-vis absorption spectra of c-melem, Mh(dehy.), Mhr, and Mhp. The vertical bars point to the wavelengths at the intersections of the dashed lines shown on the data and represent the absorption edge of each compound. The Mhp spectrum has a steep absorption edge, and the reproducibility of this spectral shape has been confirmed experimentally. Due to self-emission, the wavelength of the absorption edge of Mhp could not be quantitatively evaluated.

333 nm for c-melem and Mh(dehy.), and 335 nm for Mhr. This indicated that the absorption edges of Mhr were at slightly longer wavelengths than those of c-melem and Mh(dehy.). Due to the strong self-emitting properties of these compounds, their absorption edges could not be identified in the UV-vis spectra, especially for Mhp. The absorption edges of c-melem, Mh(dehy.), and Mhr showed very small variations. When evaluating the wavelengths of emission or absorption edges, it is necessary to understand the electronic structure of the samples as both the emission and absorption processes occur across the energy gap of the material. However, due to the random arrangement of water molecules in the channels in Mh, it was

difficult to account for this effect in energy band calculations, which limited the reliability of the calculations. Therefore, it is difficult to quantitatively compare the results of the energy band calculations with the experimental results for the difference in wavelengths of the emission and absorption edges of c-melem and Mh. The results of the energy band calculations based on DFT for c-melem and Mh are shown in Fig. S2 in the ESI.† Based on the calculations, the formation of H 1s bands in Mh was due to the alignment of water molecules in the channels, resulting in large dispersions in the ΓA and KH directions. Furthermore, since the band at the bottom of the conduction band was attributed to the H 1s band, the energy gap of Mh was significantly smaller than that of c-melem. However, in reality, we should assume that the water molecules in Mh do not form H 1s bands due to their random coordination. Without considering the energy band caused by water molecules in the Mh channels, the band at the top of the valence band could be derived from the N $2p_z$ orbital, and that at the bottom of the conduction band could be derived from the C $2p_z$ orbital. In this situation, both c-melem and Mh possessed similar energy gaps (2.94 eV for c-melem and 3.28 eV for Mh). This result was consistent with the similar absorption edges of c-melem, Mh(dehy.), and Mhr depicted in the UV-vis spectra shown in Fig. 7(b).

Fig. 8(a) shows the results of the fluorescence lifetime measurements on c-melem, Mh(dehy.), Mhr, and Mhp. The time required for the emission intensity to decay to 1/1000 increased in the order of c-melem, Mh(dehy.), Mhr, and Mhp. The PL absolute quantum yields Φ and average fluorescence lifetimes, evaluated from the fluorescence lifetime measurement results in Fig. 8, are shown in Table 3. The values of Φ were measured using excitation light at a wavelength of 300 nm because, as shown in Fig. S3, (ESI†) high values were obtained for all materials under 300 nm excitation light.

Based on Table 3, Φ decreased and the fluorescence lifetime τ increased in the order of c-melem, Mh(dehy.), Mhr, and Mhp. c-Melem and Mh demonstrated very high values of Φ ranging between 65% and 80%, although there were some large and small differences between them. This could be attributed to the presence of strong hydrogen bonds and π-stacks between melem molecules in the crystal structure of these compounds, suppressing radiation-free deactivation.[62] As melem molecules are more strongly constrained in crystals than in solutions, the displacement of each atom between the ground state and the excited state after light absorption was small, and the radiation-free deactivation due to vibrational excitation was relatively suppressed. This interpretation is supported by the fact that the Φ of the DMSO s. d. solution of melem (melem(DMSO)) is less than a quarter of the value of c-melem. In other words, the τ of melem, which is not constrained like melem in crystals, is comparable to that of c-melem, yet Φ is significantly lower. Mh exhibited a lower quantum yield and a longer fluorescence lifetime than c-melem. The longer fluorescence lifetime of Mh suggested that it was relatively more prone to radiation-free deactivation. In order to explain this difference, the structure of a single melem molecule in the excited state in each crystal should be studied computationally. It is possible that the melem molecules in Mh have smaller displacements in atomic positions in the excited state. The fact that in the c-melem crystal the melem molecule has twelve hydrogen bonds with

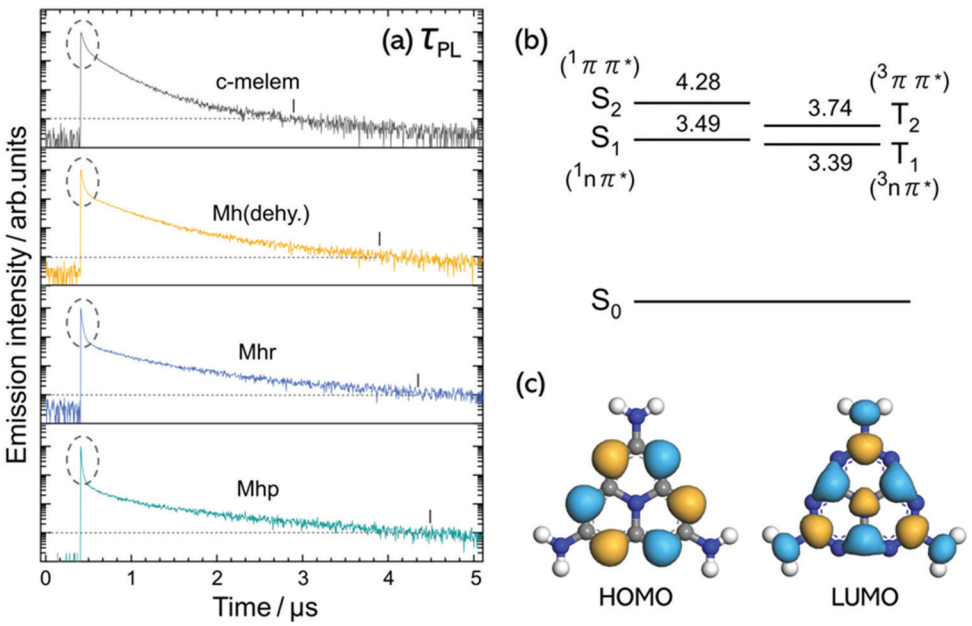

Fig. 8 (a) Fluorescence lifetime measurements on c-melem, Mh(dehy.), Mhr, and Mhp. The vertical axis is a logarithmic scale. The dashed line represents the intensity at 1/1000 of the peak value. The vertical bar on each spectrum points to the time when the intensity decays by a factor of 1000. (b) Jablonski diagram of the isolated melem molecule. The numbers represent the excited state energy measured from the ground state energy in eV. The descriptions in round brackets indicate the configuration of the molecular orbitals. (c) Wave functions of the highest occupied molecular orbital (HOMO) and the lowest unoccupied molecular orbital (LUMO) of the melem molecule. The blue and yellow parts represent different signs.

Table 3 PL absolute quantum yields Φ and average fluorescence lifetimes τ of c-melem, Mh(dehy.), Mhr, and Mhp. τ were evaluated from the fluorescence lifetime measurement results shown in Fig. 8. Melem(DMSO) refers to the DMSO s. d. solution of melem

Sample	Φ^a/%	τ^b/ns
c-Melem	80	176
Mh (dehy.)	75	287
Mhr	71	365
Mhp	65	370
Melem(DMSO)	19	161

τ is the time when the intensity decreases to $1/e$. [a] Represents the values measured using excitation light with a wavelength of 300 nm. The dependence of Φ for all the samples on the excitation light wavelength was relatively small in the excitation wavelength range of 290–310 nm except for melem(DMSO) as shown in Fig. S3 in the ESI. [b] Represents the values measured using excitation light with a wavelength of 340 nm. Emission wavelengths of 370 nm were used for measurements on c-melem, Mh(dehy.), Mhr, and melem(DMSO) while a wavelength of 380 nm was used for the measurement on Mhp.

five neighboring melem molecules, whereas in the Mh crystal the melem molecule has eight hydrogen bonds with four neighboring melem molecules, seems to support this hypothesis.[1,55]

Another factor contributing to the high quantum yields of c-melem, Mh(dehy.), Mhr, and Mhp could be qualitatively explained by the electronic structure of a single melem molecule. Fig. 8(b) shows the Jablonski diagram of a melem molecule obtained by DFT calculations. From this diagram, melem was expected to be prone to intersystem crossing from the singlet excited state S_1 to the triplet excited state T_2 by thermal excitation because S_1 and T_2 had very similar energies. Furthermore, due to the ($^1n\pi^*$) configuration of S_1 and ($^3\pi\pi^*$) configuration of T_2, the transition from S_1 to T_2 was a spin-allowed transition that occurred *via* the spin-orbit interaction, allowing the intersystem crossing from S_1 to T_2. The reverse intersystem crossing from T_2 to S_1 would then produce delayed fluorescence. As some molecules excited to T_2 would relax to T_1, reverse intersystem crossing from T_1 to S_1 could be induced easily as the S_1 and T_1 states are very close energetically, leading to the occurrence of TADF.[63,64] As shown in Fig. 8(c), the HOMO and LUMO of the melem molecule with a heterocyclic ring had a very small spatial overlap, resulting in a small exchange integral. As such, no large energy difference was observed between the S_1 and T_1 states. This proved that TADF might be one of the reasons causing the delayed fluorescence exhibited by these melem-based compounds.

A first-principle simulation study on the mechanism of proton-conjugated electron transfer (PCET) between the nitrogen atom of the heptadine (Hz) ring and the hydrogen atom of water in the complex of Hz and water has recently been reported. The results of this study suggest the photodetachment of the hydrogen bonded to the nitrogen of the Hz ring and the return of the proton to Hz when the heptadinyl radical produced after PCET is reilluminated.[65,66] Therefore, in addition to the abovementioned solid-state effects, such as hydrogen bonding and TADF, photochemical reactions may also be responsible for the high quantum yields and relatively long fluorescence lifetimes of these melem-based compounds.

3.4. Moisture absorption of Mh(dehy.) and recovery of Mh

As discussed in the results shown in Fig. 4, Mh(dehy.) was expected to exhibit hygroscopicity. In other words, Mh(dehy.), obtained by completely dehydrating Mh, could be rehydrated in air. In this study, the hygroscopicity of Mh(dehy.) was investigated by examining its structure and chemical state after being immersed in water for 1 h and left in air for 1 week. The former was referred to as Mh(dehy.)(water, 1 h) and the latter as Mh(dehy.)(atm., 1 w). In previous sections, Mh(dehy.) referred to the powder obtained by annealing Mh at 150 °C for 24 h and leaving it in air. For the study of hygroscopicity, Mh(dehy.) was prepared by annealing Mh at 150 °C for 24 h and then placing it in a container with a lid to prevent it from being exposed to the atmosphere. As such, the Mh(dehy.) produced was almost anhydrous. Based on the TG-DTA results of Mh(dehy.)(water, 1 h) and Mh(dehy.)(atm., 1 w) shown in Fig. S4 in the ESI,† the mass of Mh(dehy.)(water, 1 h) and Mh(dehy.)(atm., 1 w) decreased when the temperature was increased from room temperature to approximately 125 °C, similar to the results of Mh(dehy.) shown in Fig. 4(b). Using the decrease in mass caused by the loss of water, the molar ratio of water to the melem molecule for Mh(dehy.)(water, 1 h) and Mh(dehy.)(atm., 1 w) was calculated to be 0.83 (percentage of the mass of water absorbed: 6.39%) and 0.58 (percentage of the mass of water absorbed: 4.59%), respectively. Since more water molecules were incorporated into Mh(dehy.)(water, 1 h) than into Mh(dehy.)(atm., 1 w), Mh(dehy.) was proven to show moisture-absorbing abilities.

The XRD profile of Mh(dehy.) in Fig. 9(a) shows that the peak due to interlayer diffraction appearing at 2θ = 25–28° collapsed, and the (300) diffraction characteristic of Mh, which should appear at around 2θ = 10°, was hardly seen. This indicated that the crystal structure of Mh was significantly disrupted by dehydration. However, the results in Fig. 7(a) show that as the amount of water incorporated into the crystal increased, both the in-plane and out-of-plane diffraction peaks became narrower, and the spectral intensity increased to match the profile of Mh shown in Fig. 2.

The absorption caused by the stretching vibration of the NH group at 3427 and 3487 cm^{-1} in the FTIR spectra shown in Fig. 9(b), as indicated by the gray dashed lines, was also observed in the FTIR spectrum of c-melem shown in Fig. 3(a). This indicated that Mh(dehy.) was almost completely dehydrated. In contrast, these absorptions were weak and only slightly observed in the FTIR spectrum of Mh(dehy.)(atm., 1 w). In the FTIR spectrum of Mh(dehy.)(water, 1 h), these two characteristic peaks disappeared completely, but the absorption due to the stretching vibration of the NH group hydrogen-bonded to the water molecule, which is characteristic of hydrates, was clearly observed.

These results showed that the stable packing of Mh(dehy.) could be restored after absorbing water. In other words, Mh was shown to be resistant to humidity in the atmosphere, and even if it dehydrates, it could take in water from the atmosphere to repair its structure.

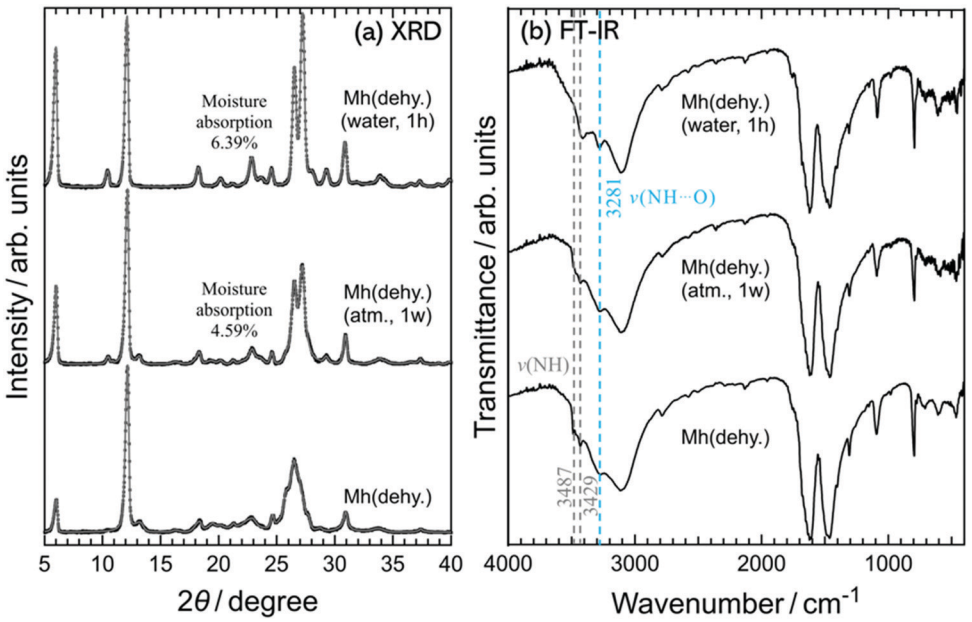

Fig. 9 (a) Changes in XRD profiles and (b) FTIR spectra of Mh(dehy.) when it was left in water for 1 h (Mh(dehy.)(water, 1 h)) and in air for a week (Mh(dehy.)(atm., 1 w)). The percentage value in (a) represents the mass of water absorbed, as determined from TG-DTA measurements. The Mh(dehy.) sample as a starting material was completely dehydrated and was not affected by the moisture in air.

4. Conclusions

In this study, we reported the growth and characterization of single crystals of Mh, and performed a detailed study on their optical properties and hygroscopicity. Mhr, a hexagonal prismatic single crystal of Mh, measuring several tens of micrometers in length, was successfully grown by precisely adjusting the water content during the hydration process. The cross-sectional length of the crystal was over several micrometers, easing the attachment of electrodes to the crystal, and thus opening up the possibility of its application in optoelectronic devices. In addition, the XRD results showed that the crystal structure of the Mh single crystal was greatly disrupted by intentional dehydration. The SEM images also suggested that the hexagonal prisms of the Mh single crystal were twisted after dehydration. However, Mr(dehy.) was hygroscopic and could absorb moisture in air, restoring the crystal structure of Mh over a long period of time. While the detailed mechanism of this recovery is yet to be understood, it indicates that the Mh crystals were resistant to humidity. In addition, a new compound of Mh with different amounts of water was discovered, and its crystal structure, optical property, and thermal behavior were different from those of c-melem and Mh.

Mh showcased a high absolute quantum yield of fluorescence, similar to that of c-melem, which was found to be due to delayed fluorescence. However, compared to c-melem, Mh exhibited changes such as longer delay times, indicating that differences in the crystal structure or hydrogen bonding with water molecules affected the luminescence of the crystals.

Understanding the fundamental properties of Mh would provide insight into the role of hydrogen bonding in crystal formation and the fundamental properties of CN compounds. Such information enables the understanding of the electronic structures of CN compounds, aiding their application as photocatalysts and optoelectronic devices.

Conflicts of interest

There are no conflicts to declare.

Acknowledgements

The authors would like to thank Prof. S. Yoshioka of TUS for assistance with the SEM measurements.

References

1 S. J. Makowski, P. Köstler and W. Schnick, *Chem. – Eur. J.*, 2012, **18**, 3248–3257, DOI: **10.1002/chem.201103527**.
2 V. W.-H. Lau and B. V. Lotsch, *Adv. Energy Mater.*, 2022, **12**, 2101078, DOI: **10.1002/aenm.202101078**.
3 X. Wang, K. Maeda, A. Thomas, K. Takanabe, G. Xin, J. M. Carlsson and K. Domen, *Nat. Mater.*, 2009, **8**, 76–80, DOI: **10.1038/nmat2317**.
4 A. Thomas, A. Fischer, F. Goettmann, M. Antonietti, J. O. Müller, R. Schlögl and J. M. Carlsson, *J. Mater. Chem.*, 2008, **18**, 4893–4908, DOI: **10.1039/b800274f**.
5 A. Wang, X. Zhang and M. Zhao, *Nanoscale*, 2014, **6**, 11157–11162, DOI: **10.1039/c4nr02707h**.
6 B. V. Lotsch, M. Döblinger, J. Sehnert, L. Seyfarth, J. Senker, O. Oeckler and W. Schnick, *Chem. – Eur. J.*, 2007, **13**, 4969–4980, DOI: **10.1002/chem.200601759**.

7 G. Algara-Siller, N. Severin, S. Y. Chong, T. Björkman, R. G. Palgrave, A. Laybourn, M. Antonietti, Y. Z. Khimyak, A. V. Krasheninnikov and J. P. Rabe, *Angew. Chem., Int. Ed.*, 2014, **53**, 7450–7455, DOI: **10.1002/anie.201402191**.
8 B. Jürgens, E. Irran, J. Senker, P. Kroll, H. Müller and W. Schnick, *J. Am. Chem. Soc.*, 2003, **125**, 10288–10300, DOI: **10.1021/ja0357689**.
9 D. L. Yu, J. L. He, Z. Y. Liu, B. Xu, D. C. Li and Y. J. Tian, *J. Mater. Sci.*, 2008, 689–695, DOI: **10.1007/s10853-007-2148-y**.
10 V. W.-H. Lau, I. Moudrakovski, T. Botari, S. Weinberger, M. B. Mesch, V. Duppel, J. Senker, V. Blum and B. V. Lotsch, *Nat. Commun.*, 2016, **7**, 12165, DOI: **10.1038/ncomms12165**.
11 F. Fina, S. K. Callear, G. M. Carins and J. T.-S. Irvine, *Chem. Mater.*, 2015, **27**, 2612–2618.
12 T. Tyborski, C. Merschjann, S. Orthmann, F. Yang, M. C. Lux-Steiner and T. Schedel-Niedrig, *J. Phys.: Condens. Matter*, 2013, **25**, 395402.
13 K. Akaike, K. Aoyama, S. Dekubo, A. Onishi and K. Kanai, *Chem. Mater.*, 2018, **30**, 2341–2352, DOI: **10.1021/acs.chemmater.7b0531**.
14 H. Inoki, G. Seo and K. Kanai, *Appl. Surf. Sci.*, 2020, **534**, 147569, DOI: **10.1016/j.apsusc.2020.147569**.
15 Y. Zhang, Q. Pan, G. Chai, M. Liang, G. Dong, Q. Zhang and J. Qiu, *Sci. Rep.*, 2013, **3**, 1–8, DOI: **10.1038/srep01943**.
16 Y. Miyake, G. Seo, K. Matsuhashi, N. Takada and K. Kanai, *Mater. Adv.*, 2021, **2**, 6083–6093, DOI: **10.1039/d1ma00579k**.
17 H. B. Zheng, W. Chen, H. Gao, Y. Y. Wang, H. Y. Guo, S. Q. Guo, Z. L. Tang and J. Y. Zhang, *J. Mater. Chem. C*, 2017, **5**, 10746–10753, DOI: **10.1039/c7tc02966g**.
18 H. Zheng, Z. Zhao, J. B. Phan, H. Ning, Q. Huang, R. Wang, J. Zhang and W. Chen, *ACS Appl. Mater. Interfaces*, 2020, **12**, 2145–2151, DOI: **10.1021/acsami.9b19915**.
19 J. Ehrmaier, E. J. Rabe, S. R. Pristash, K. L. Corp, C. W. Schlenker, A. L. Sobolewski and W. Domcke, *J. Phys. Chem. A*, 2019, **123**, 8099–8108, DOI: **10.1021/acs.jpca.9b06215**.
20 J. Li, L. Tao, Y. Wang, Y. Yao and Q. Guo, *Front. Chem.*, 2021, **9**, 1–7, DOI: **10.3389/fchem.2021.717569**.
21 J. Li, Q. Zhang, H. Nomura, H. Miyazaki and C. Adachi, *Appl. Phys. Lett.*, 2014, **105**, 1–5, DOI: **10.1063/1.4887346**.
22 K. Aoyama, K. Akaike and K. Kanai, *Chem. Phys. Lett.*, 2020, **749**, 137475, DOI: **10.1016/j.cplett.2020.137475**.
23 A. Rezaie, G. Y. Melmed, G. Leite, R. Mathur, W. Takakura, I. Pedraza, M. Lewis, R. Murthy, G. Chaux and M. Pimentel, *Adv. Ther.*, 2021, **38**, 4556–4568, DOI: **10.1007/s12325-021-01830-7**.
24 J. Na, S. Bi, C. Jiang and J. Song, *Org. Electron.*, 2020, **82**, 105718, DOI: **10.1016/j.orgel.2020.105718**.
25 X. Yuan, K. Luo, N. Liu, X. Ji, C. Liu, J. He, G. Tian, Y. Zhao and D. Yu, *Phys. Chem. Chem. Phys.*, 2018, **20**, 20779–20784, DOI: **10.1039/c8cp01550c**.
26 N. Liu, T. Li, Z. Zhao, J. Liu, X. Luo, X. Yuan, K. Luo, K. Luo, J. He, D. Yu and Y. Zhao, *ACS Omega*, 2020, **5**, 12557–12567, DOI: **10.1021/acsomega.0c01607**.
27 E. W. Hughes, *Am. Chem. Soc.*, 1941, **63**, 1737, DOI: **10.1021/ja01851a069**.
28 A. Schwarzer, T. Saplinova and E. Kroke, *Coord. Chem. Rev.*, 2013, **257**, 2032–2062, DOI: **10.1016/j.ccr.2012.12.006**.
29 P. J. Larkin, M. P. Makowski and N. B. Colthup, *Spectrochim. Acta, Part A*, 1999, **55**, 1011–1020, DOI: **10.1016/S1386-1425(98)00244-3**.
30 L. Yang, X. Liu, Z. Liu, C. Wang, G. Liu and Q. Li, *Ceram. Int.*, 2018, **44**, 20613–20619, DOI: **10.1016/j.ceramint.2018.06.105**.
31 Y. Wang, N. Wu, C. Liu, M. K. Albolkany, M. Wang, Y. Wang, S. Arooj, W. Zhang and B. Liu, *Mater. Horiz.*, 2020, 149–156, DOI: **10.1039/c9mh00521h**.
32 T. Li, B. T. Liu, Z. B. Fang, Q. Yin and R. Wang, *J. Mater. Chem. A*, 2021, **9**, 4687–4691, DOI: **10.1039/d1ta00100k**.
33 Z. Huang, F. W. Yan and G. Q. Yuan, *ACS Sustainable Chem. Eng.*, 2018, **6**, 3187–3195, DOI: **10.1021/acssuschemeng.7b03305**.
34 G. Zhao, G. Liu, H. Pang, H. Liu, H. Zhang, K. Chang, X. Meng, X. Wang and J. Ye, *Small*, 2016, **12**, 6160–6166, DOI: **10.1002/smll.201602136**.
35 S. Li, Z. Wang, X. Wang, F. Sun, K. Gao, N. Hao, Z. Zhang, Z. Ma, H. Li, X. Huang and W. Huang, *Nano Res.*, 2017, **10**, 1710–1719, DOI: **10.1007/s12274-017-1423-8**.
36 P. Li, M. R. Ryder and J. F. Stoddart, *Acc. Mater. Res.*, 2020, **1**, 77–87, DOI: **10.1021/accountsmr.0c00019**.
37 A. Ranganathan, V. R. Pedireddi and C. N.-R. Rao, *J. Am. Chem. Soc.*, 1999, **121**, 1752–1753, DOI: **10.1021/ja983928o**.
38 X. Zhao, T. Liu, Y. Cui, X. Hou, Z. Liu, X. Dai, J. Kong, W. Shi and T. J.-S. Dennis, *Nanoscale*, 2018, **10**, 8170–8179, DOI: **10.1039/c8nr01305e**.
39 X. Zhao, T. Liu, Y. Zhang, S. Wang, X. Li, Y. Xiao, X. Hou, Z. Liu, W. Shi and T. J.-S. Dennis, *Adv. Mater. Interfaces*, 2018, **5**, 1–9, DOI: **10.1002/admi.201800336**.
40 R. Ding, J. Feng, F. Dong, W. Zhou, Y. Liu, X. Zhang, X. Wang, H. Fang, B. Xu and Z. Li, *et al.*, *Adv. Funct. Mater.*, 2007, 1604659, DOI: **10.1002/adfm.201604659**.
41 H. Nakanotani, M. Saito, H. Nakamura and C. Adachi, *Appl. Phys. Lett.*, 2009, **95**, 033308, DOI: **10.1063/1.3184588**.
42 T. Takahashi, T. Takenobu, J. Takeya and Y. Iwasa, *Adv. Funct. Mater.*, 2007, **17**, 1623–1628, DOI: **10.1002/adfm.200700046**.
43 H. Nakanotani, M. Saito, H. Nakamura and C. Adachi, *Appl. Phys. Lett.*, 2009, **95**, 103307, DOI: **10.1063/1.3216047**.
44 Y. Yomogida, T. Takenobu, H. Shimotani, K. Sawabe, S. Z. Bisri, T. Yamao, S. Hotta and Y. Iwasa, *Appl. Phys. Lett.*, 2010, **97**, 1–4, DOI: **10.1063/1.3504690**.
45 H. Jiang and C. Kloc, *MRS Bull.*, 2013, **38**, 27–33, DOI: **10.1557/mrs.2012.308**.
46 Y. Dang, D. Ju, L. Wang and X. Tao, *CrystEngComm*, 2016, **18**, 4476–4484, DOI: **10.1039/c6ce00655h**.
47 J. Di, J. Chang and S. (Frank) Liu, *EcoMat*, 2020, **2**, 1–24, DOI: **10.1002/eom2.12036**.
48 L. M. Pedroso, M. M.-C. A. Castro and P. Simões, *Polymer*, 2005, **46**, 1766–1774, DOI: **10.1016/j.polymer.2004.12.046**.
49 H. Wang, 2013, DOI: **10.5282/edoc.16549**.
50 H. Zuo, Y. Li and Y. Liao, *ACS Appl. Mater. Interfaces*, 2019, **11**, 39201–39208, DOI: **10.1021/acsami.9b14795**.
51 A. Sattler and W. Schnick, *Z. Anorg. Allg. Chem.*, 2006, **632**, 238–242, DOI: **10.1002/zaac.200500363**.

52 S. J. Clark, M. D. Segall, C. J. Pickard, P. J. Hasnip, M. I.-J. Probert, K. Refson and M. C. Payne, *Z. Kristallogr.*, 2005, **220**, 567–570, DOI: **10.1524/zkri.220.5.567.65075**.

53 J. P. Perdew, K. Burke and M. Ernzerhof, *Phys. Rev. Lett.*, 1996, **77**, 3865, DOI: **10.1103/PhysRevLett.77.3865**.

54 J. Kim, C. Park and H. C. Choi, *Chem. Mater.*, 2005, **27**, 2408–2413, DOI: **10.1021/cm5044478**.

55 B. Jürgens, E. Irran, J. Senker, P. Kroll, H. Müller and W. Schnick, *J. Am. Chem. Soc.*, 2003, **125**, 10288–10300, DOI: **10.1021/ja0357689**.

56 H. B. Zheng, W. Chen, H. Gao, Y. Y. Wang, H. Y. Guo, S. Q. Guo, Z. L. Tang and J. Y. Zhang, *J. Mater. Chem. C*, 2017, **5**, 10746–10753, DOI: **10.1039/c7tc02966g**.

57 K. Balakrishnan, A. Datar, R. Oitker, H. Chen, J. Zuo and L. Zang, *J. Am. Chem. Soc.*, 2005, **127**, 10496–10497, DOI: **10.1021/ja052940v**.

58 C. Park, E. Yoon, M. Kawano, T. Joo and H. C. Choi, *Angew. Chem., Int. Ed.*, 2010, **49**, 9670–9675, DOI: **10.1002/anie.201005076**.

59 J. Kim, C. Park and H. C. Choi, *Chem. Mater.*, 2005, **27**, 2408–2413, DOI: **10.1021/cm5044478**.

60 C. Yang, K. Folens, G. Du Laing, F. Artizzu and R. Van Deun, *Adv. Funct. Mater.*, 2020, **30**, 1–10, DOI: **10.1002/adfm.202003656**.

61 K. Park, Y. Kim and K. J. Lee, *J. Radioanal. Nucl. Chem.*, 2019, **322**, 487–493, DOI: **10.1007/s10967-019-06734-z**.

62 Y. Gong, L. Zhao, Q. Peng, D. Fan, W. Z. Yuan, Y. Zhang and B. Z. Tang, *Chem. Sci.*, 2015, **6**, 4438–4444, DOI: **10.1039/c5sc00253b**.

63 Y. Im, M. Kim, Y. J. Cho, J. A. Seo, K. S. Yook and J. Y. Lee, *Chem. Mater.*, 2017, **29**, 1946–1963, DOI: **10.1021/acs.chemmater.6b05324**.

64 H. Uoyama, K. Goushi, K. Shizu, H. Nomura and C. Adachi, *Nature*, 2012, **492**, 234–238, DOI: **10.1038/nature11687**.

65 J. Ehrmaier, T. N.-V. Karsili, A. L. Sobolewski and W. Domcke, *J. Phys. Chem. A*, 2017, **121**, 4754–4764, DOI: **10.1021/acs.jpca.7b04594**.

66 D. Hwang and C. W. Schlenker, *Chem. Commun.*, 2021, **57**, 9330–9353, DOI: **10.1039/d1cc02745j**.